

## JOINT ANALYSIS OF GYRAL FOLDING AND FIBER SHAPE PATTERNS

Xiang Yu<sup>1</sup>\*, Hanbo Chen<sup>2</sup>\*, Tuo Zhang<sup>1,2</sup>, Xintao Hu<sup>1</sup>, Lei Guo<sup>1</sup>, Tianming Liu<sup>2</sup>

<sup>1</sup>School of Automation, Northwestern Polytechnical University, Xi'an, China; <sup>2</sup>Cortical Architecture Imaging and Discovery Lab, Department of Computer Science and Bioimaging Research Center, The University of Georgia, Athens, GA, USA;

\*These authors contributed equally to this work.

### ABSTRACT

Cortical gyral folding pattern can be described by the hinge numbers, e.g., 2-hinge and 3-hinge gyri. Our recent studies have shown that joint analysis of 2-hinge gyral folding and its fiber connection patterns can be a powerful tool to elucidate the regularity and variability of gyral structures. However, other more complex gyral shape patterns such as 3-hinge gyri have not been investigated yet. In this paper, we proposed a novel computational framework to characterize 3-hinge gyral folding patterns and jointly analyze the correlation between folding and DTI-derived fiber orientation patterns in these regions. To characterize and differentiate these 3-hinge gyral folding patterns, an effective decision tree model is designed and applied to classify these 3-hinge gyral patches into the combinations of five basic sub-types of 'S', 'U', 'V', 'I', and other shapes. Then, the correlations between the shapes of these sub-types of 3-hinge gyri and their DTI-derived fiber connection patterns are quantitatively assessed, and our results demonstrated their close relationships. This work further replicated and strengthened our previous finding obtained in 2-hinge gyri that gyral folding patterns are closely correlated with fiber connection patterns.

**Index Terms**—folding pattern, shape analysis, DTI, MRI

### 1. INTRODUCTION

It has been reported that cortical gyral folding pattern can be effectively described by the hinge numbers [1]. As shown in Fig. 1(b), a gyral hinge field is the region on top of gyrus with the maximal folding curvature. When connecting hinge fields along a gyrus, a gyral hinge line can be obtained and multiple hinge lines will meet at the cross-point (Fig. 1b). Therefore, for a hinge field on a gyrus, the number of hinge lines connecting to this field can be used to describe the folding pattern of this gyrus [1]. As shown in Fig. 1(a), in an example of human brain cerebral cortex, we can identify 2-hinge, 3-hinge, and 4-hinge gyri [1]. A quantitative approach to identifying those n-hinge ( $n=2, 3, 4$ ) gyri via surface profiling was detailed in our prior publication [1].

In addition to the number of hinges on gyri, the shape of hinge line can also be used to describe the local cortical gyral folding pattern, e.g., measuring the convoluted shape of gyrus. In our recent work in [2], this measurement has been applied to describe the folding pattern of certain gyri on the cortex including Superior Frontal Gyrus (SFG), Precentral Gyrus (preCG), Postcentral Gyrus (postCG), and Superior Temporal Gyrus (STG). In particular, the joint analysis of gyral folding pattern and fiber orientation patterns on these gyri demonstrated strong positive correlations, which further supported our finding in [3] that significantly denser DTI-derived fibers are connected to the gyral regions than sulcal regions. However, the results in [2] were based only on 2-hinge

gyri (Fig. 2a) and the relationships between gyral folding and fiber connection patterns for 3-hinge gyri have not been examined in more complex gyral regions such as 3-hinge gyri (Fig. 2b) yet.

In this paper, we proposed a novel computational framework to characterize 3-hinge gyral folding patterns and jointly analyze the correlation between folding and fiber orientation patterns in these regions. To quantitatively characterize and differentiate these 3-hinge gyral folding patterns, an effective and novel decision tree model is designed and applied to classify these 3-hinge gyral patches into the combinations of five basic sub-types of 'S', 'U', 'V', 'I', and other shapes. Then, the correlations between the shapes of these sub-types of 3-hinge gyri and their DTI-derived fiber connection patterns are quantitatively assessed respectively, and our results demonstrated their close relationships. This work further replicated and strengthened our previous finding obtained in 2-hinge gyri that gyral folding patterns are closely correlated with fiber connection patterns [2].

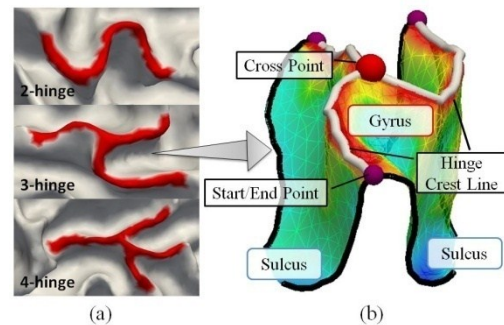


Fig. 1. (a) Example of 2-hinge, 3-hinge, and 4-hinge gyri, from the top to the bottom. (b) Illustration of gyral hinge crest line, start/end point, and cross point on a 3-hinge example.

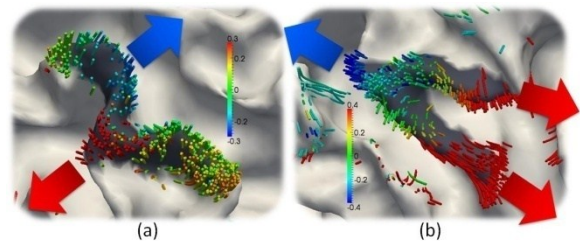


Fig. 2. Illustration of the close relationship between fiber orientation (colored dots) and gyral folding (colored arrows). (a)- (b): examples of 2-hinge gyri and 3-hinge gyri, respectively.

### 2. METHODS

#### 2.1. Gyral Hinge Extraction

We extracted 3-hinge gyri and performed gyral folding pattern analysis on the reconstructed cortical surface [4]. Before joint

analysis, a 3-hinge gyrus is first decomposed into three hinge lines (Fig. 3a). Here, the cross point (Fig. 1b) of a 3-hinge is picked with the assistance of ParaView [5]. Then a patch of 3-hinge gyrus can be obtained by expanding to the neighboring regions of the cross point on the cortical surface. After that, the surface patch is rotated such that the z-axis direction is the same as the average normal direction of the patch. In this way, the z value of the coordinate of a vertex on the patch can be viewed as the altitude of that vertex (Fig. 3b). If we extract the altitude value along the boundary of a 3-hinge gyrus patch, 3 peaks can be observed, which correspond to the points on hinge lines (Fig. 3b-c). By setting these points as the start/end points (Fig. 1b) and the cross point as the transit point, a fast matching algorithm [6] is applied to obtain these hinge lines.

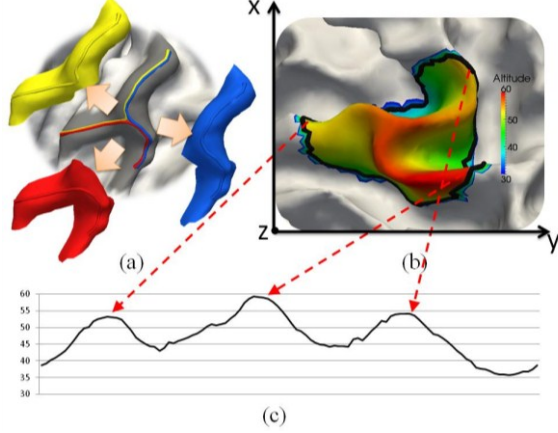


Fig. 3. Illustration of 3-hinge extraction and decomposition. (a) Decompose a 3-hinge gyrus into three hinge lines. (b) An example of gradient map of altitude in the local coordinate system of a patch. (c) Altitude curve of boundary of patch in (b).

## 2.2. Hinge Line Shape Features

Before measuring the hinge shape, we project the hinge line to the x-y plan of a local coordinate system of the gyral patch defined previously (Fig. 3b). Then, the number of points in each line is resampled to the same number  $n$ , which is empirically set as 50 in this paper. Each hinge line is also rescaled such that the overall length is 100 points for the purpose of comparison. Based on this set-up, two sets of features are computed to quantitatively measure the shapes of hinge lines as follows.

We used the average determinant of the orientation matrix defined in [2] as a measurement of curvedness of a hinge line. For a node  $i$  on the hinge line  $L$ , its curvedness  $c_i$  is defined as:

$$c_i = \frac{\sum_{j=i-w}^{j=i+w} \det(O(i, j, L))}{2w+1} \quad (1)$$

where  $w$  is the window width,  $\det(O(i, j, L))$  is the determinant of orientation matrix [2]. In [2], it has been shown that this feature can be used as a simple yet efficient measurement of the line shapes and can be applied in the joint analysis of fiber shapes and gyral folding patterns. Essentially, it carries the local curvature information, orientation information of a gyral hinge line and it is robust to noise. Examples are shown in Fig. 4.

We used the distance between the end node and start node of a hinge line as a measurement of its straightness. Since we have rescaled the hinge line to a unit length, for a straight line, the distance between its two ends will be close to 1. On the contrary, for a highly bended line, the distance will be relatively small. Examples are shown in Fig. 4.

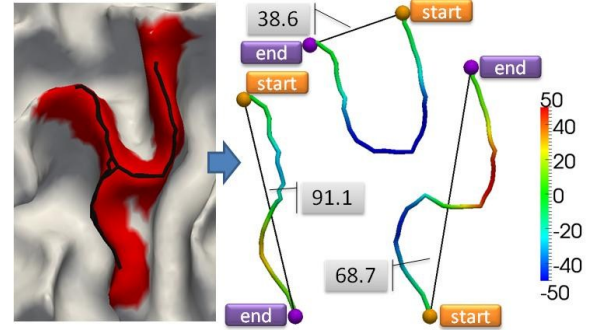


Fig. 4. An example of hinge line features. Each line is color-coded by its curvedness (color bar is on the right side). The distance between the end and start nodes is shown.

## 2.3. Gyral Shape Classification Model

By our extensive observations, 4 major sub-types can be recognized for the hinge lines including ‘S’, ‘U’, ‘V’, and ‘I’ shapes (Fig. 5b). For ‘S’ shape, the hinge line bends to the opposite directions on two sides of the cross point. For ‘U’ and ‘V’ shapes, the hinge line bends at the center of the hinge line. However, for ‘V’ shape, the two ends of a hinge line are more open compared with the ‘U’ shape. For ‘I’ shape, the hinge line is relatively straight. Some other shapes can also be observed such as ‘W’ (bend to the same direction on two sides of cross point) or ‘J’ (one side is bend, the other side is straight). However, these shapes can rarely be observed compared with previous four sub-types, thus we classify them as ‘other’ shape (‘O’ for short).

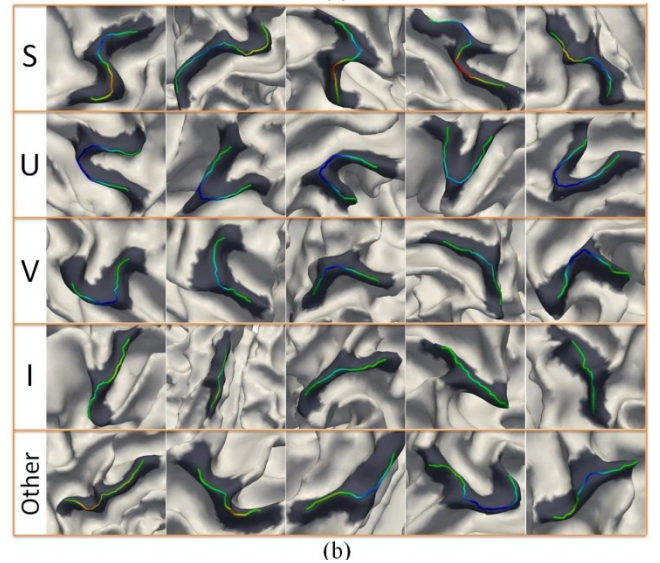
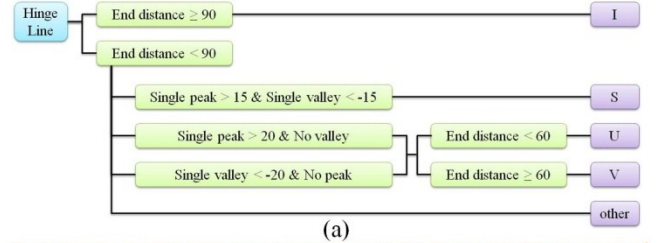


Fig. 5. (a) The decision tree model. (b) Example of 5 sub-types of hinge line.



Based on the above-mentioned features and extensive empirical observations, a decision tree is designed and applied to classify these hinge lines, as shown in Fig. 5(a). The decision is made based on the extrema of line curve and the distance between two ends. For the extrema of line curve, only the local maximum value (peak) and local minimum value (valley) with absolute value larger than 1 are considered. Examples of shapes obtained via the decision tree are shown in Fig. 5(b).

## 2.4. Fiber Orientation

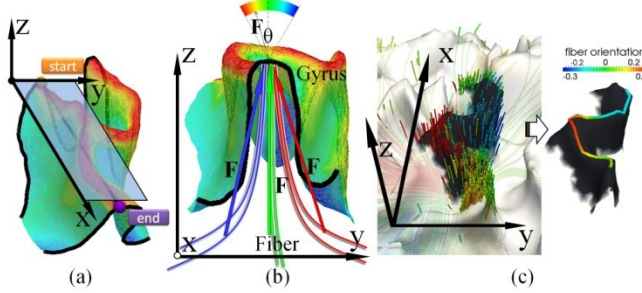


Fig. 6. (a) Definition of gyral local coordinate system. Z-axis follows the norm direction of the hinge patch. X-axis points from the start side to the end side of gyrus. (b) Definition of fiber orientation. (c) An example of projecting the fiber orientations to the hinge line.

We defined the fiber orientation as its principal direction on the side that the fiber intersects with a hinge (Fig. 6(b)). Then, the entropy  $H$  of a bundle of fibers that intersect with a hinge is defined based on the distribution of fibers' orientations on the unit sphere [7].

$$H(F) = -\sum_{i=1}^n P(f_i) \log P(f_i) \quad (2)$$

where  $F$  is the fiber bundle,  $P(f_i)$  is the probability of certain orientation of fiber  $i$ . The larger the entropy is, the less consistent the orientations of fibers will be.

For the joint analysis with gyral shape pattern, we project the local orientations of fibers along the hinge line to the perpendicular direction. First, a local coordinate system is defined for each hinge line as shown in Fig. 6(a). Then, the shape pattern for each fiber is defined as the angle between the z-axis and the local orientation of its projection on y-z plan ( $\theta$  in Fig. 6(b)). Then, we can project the obtained fiber orientation to the hinge line, as shown in Fig. 6(c). Later, this projected value can be compared with the hinge line curve for joint analysis.

## 3. RESULTS

### 3.1. Experiment Data and Preprocessing

Sixteen healthy adult volunteers were recruited for this study. DTI data was acquired: spatial resolution  $2 \times 2 \times 2 \text{ mm}^3$ , matrix size  $128 \times 128$ , 60 slices,  $TR=15.5s$ ,  $TE=\text{min-full}$ ,  $b\text{-value}=1000$  with 30 DWI gradient directions and 3 B0 volumes acquired. T1-weighted MRI images were also acquired:  $TE=\text{min-full}$ ,  $TR=7.5 \text{ ms}$ , flip angle  $=20^\circ$ , 154 axial slices, slice thickness  $=1.2 \text{ mm}$ , and  $FOV=256 \times 256 \text{ mm}$ . Preprocessing is similar to the method in [2]. For the anatomic data, pre-processing included brain skull removal, GM(gray matter)/WM(white matter) tissue segmentations [8], GM/WM cortical surfaces reconstruction [4], and linear registration to DTI space [9]. For the DTI data, pre-processing included brain skull removal, motion correction, eddy current

correction, and fiber tractography [2], [3]. All the 3-hinges located on 4 brain regions (Table I) of both brain hemispheres are picked by experts via the ParaView.

### 3.2. Gryal Shape Patterns

In total, 92 3-hinge gyri are delineated and processed via our algorithmic framework. Totally, 276 hinge lines were automatically extracted from the 92 3-hinge gyri and then classified into 5 sub-types (Fig. 5b). The 4 major sub-types of shapes cover 86.6% of all hinge lines. The number of 3-hinge gyrus and each sub-type in each region is counted and listed in Table I. An intriguing observation is that the number of 3-hinge gyri on the Precentral Gyrus is more than those on other regions we analyzed. Another interesting observation is that among the 4 major sub-types of hinge lines, the number of 'S' shape is the largest and the number of 'I' shape is the least. This result indicates that gyri in 3-hinge regions are really convoluted, which is a major shape characteristic of the cerebral cortex.

Table I. Numbers of 3-hinge gyri and sub-types in each brain region. 3H: 3-Hinge; O: other shapes.

	3H	S	U	V	I	O
Total	92	84	50	60	45	37
Superior Frontal Gyrus	22	25	12	13	10	6
preCentral Gyrus	41	33	19	34	20	17
postCentral Gyrus	17	15	11	11	5	9
Parietal Lobule	12	11	8	2	10	5

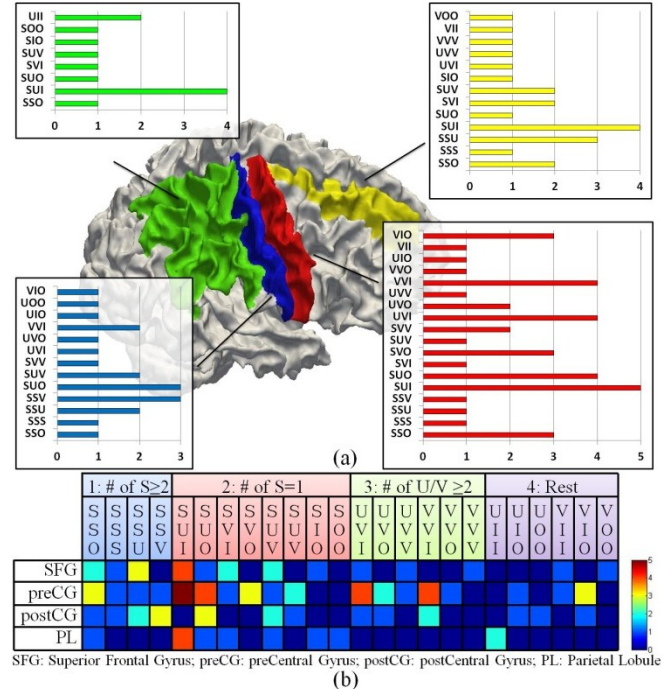


Fig. 7. Distribution of combination patterns of 3-hinge gyri in four brain areas. (a) Visualization of the combination pattern distributions on brain areas. (b) A quantitative matrix of the frequencies of combination patterns in four brain areas. The shape of 3-hinge folding shape is described by a combination of the sub-types of hinge lines. The first (1), second (2), third (3) and fourth (4) categories are in the blue, red, green and purple panels, respectively.

As each 3-hinge gyrus is composed of 3 hinge lines, the shape of a 3-hinge gyrus can be described by the combination of the sub-types of these hinge lines. We listed the number of all possible combinations among the 92 3-hinge gyri and their distributions on the cerebral cortex in Fig. 7. For annotation purpose, we used the combination of letters of the hinge line sub-types to represent the combination pattern of 3-hinge gyri. For example, SSO indicates that the 3-hinge gyri is composed by two ‘S’ shape hinge lines and one ‘other’ shape hinge line. Examples of the major 3-hinge combination patterns are visualized in Fig. 8. To facilitate conceptual understanding, we classified these 3-hinge gyri into four categories (Fig. 7b) and highlighted them with different colors in Fig. 7(b) and Fig. 8. It is evident that the category 1 3-hinge gyri have the most complex folding pattern. On the contrary, the category 2 gyri is also more convoluted than the category 3. By visual observations, it is intriguing that most of the 3-hinge gyri on SFG and the Parietal Lobule are of category 1 and category 2, and they are more convoluted. This is in good agreement with current neuroscience knowledge that the frontal lobe is more anatomically variable. In contrast, most of category 3 3-hinge gyri are located on the Central Gyri.

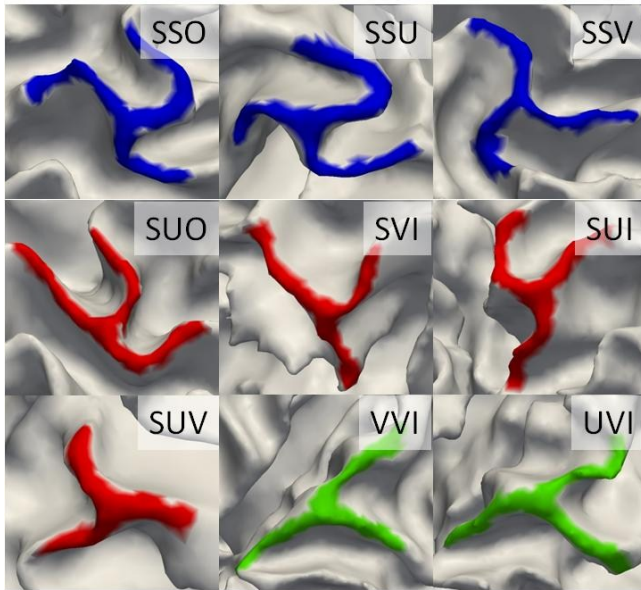


Fig. 8. Example of major combination patterns of 3-hinge gyri (colored by categories). Categories are defined in Fig. 7(b).

### 3.3. Joint Analysis

We computed the entropy of the orientations of fibers that intersect with each hinge line as described in section 2.4. They were compared between the hinge lines with different shapes. The average entropies of the fiber orientation for each sub-type of hinge line from the highest to lowest are: ‘S’/3.19; ‘O’/3.14; ‘U’/3.07; ‘V’/3.03; ‘I’/2.98. As we know, the ‘S’ shape and ‘O’ shape are more convoluted compared with the ‘I’ shape. This result agrees with our previous observation across species [2] which suggests that there may exist close correlation between DTI-derived axonal fibers’ pattern and gyral shapes – higher complexity in fiber connection pattern will result in more convoluted gyral shape [2].

We then computed the Pearson correlation between the gyral hinge lines curvedness described in section 2.2.1 and the fiber orientation along the hinge line described in section 2.4. The

average correlations for sub-types of hinge lines are relatively high except for ‘I’ shape: ‘U’/0.84; ‘O’/0.66; ‘S’/0.61; ‘V’/0.59; ‘I’/0.24. This result indicates that for those convoluted gyri, the fiber orientation and hinge curve are strongly positively correlated, which agrees with our previous observation on the 2-hinge gyri [2] that DTI-derived fibers bend to the convex direction of a gyrus.

## 4. DISCUSSION AND CONCLUSION

In this paper, we presented a novel computational framework to characterize the gyral folding pattern of 3-hinge gyri and its correlation with axonal fiber orientations. The proposed framework has been performed on 16 individuals and 92 3-hinge gyri of 4 selected brain regions. Quantitative analysis result suggests that the Superior Frontal Gyrus and Parietal Lobule are more convoluted than the Precentral Gyrus and Postcentral Gyrus. The joint analysis demonstrated the positive correlation between gyral folding patterns of 3-hinge gyri and their fibers’ orientation patterns. This agrees with our previous observations on 2-hinge gyri [2] and offers further support to our recent hypothesis that the ‘pushing’ mechanism of axonal wiring is a determinant in the neocortex folding process during fetus brain development [3]. In the future, the proposed computational framework will be used to study cortical regularity and variability in abnormal brains to unveil the causal relationship of axonal wiring and cortical folding.

## 5. REFERENCES

- [1] K. Li, L. Guo, G. Li, J. Nie, C. Faraco, G. Cui, Q. Zhao, L. S. Miller, and T. Liu, “Gyral folding pattern analysis via surface profiling,” *NeuroImage*, vol. 52, no. 4, pp. 1202–14, Oct. 2010.
- [2] H. Chen, T. Zhang, L. Guo, K. Li, X. Yu, L. Li, X. Hu, J. Han, X. Hu, and T. Liu, “Coevolution of Gyral Folding and Structural Connection Patterns in Primate Brains,” *Cerebral cortex (New York, N.Y. : 1991)*, in press, May 2012.
- [3] J. Nie, et al., “Axonal Fiber Terminations Concentrate on Gyri,” *Cerebral cortex (New York, N.Y. : 1991)*, vol. 22, no. 12, pp. 2831–9, Dec. 2012.
- [4] T. Liu, J. Nie, A. Tarokh, L. Guo, and S. T. C. Wong, “Reconstruction of central cortical surface from brain MRI images: method and application,” *NeuroImage*, vol. 40, no. 3, pp. 991–1002, Apr. 2008.
- [5] A. Henderson, “The ParaView guide : A Parallel visualization application,” 2007.
- [6] G. Li, L. Guo, J. Nie, and T. Liu, “An automated pipeline for cortical sulcal fundi extraction,” *Medical image analysis*, vol. 14, no. 3, pp. 343–59, Jun. 2010.
- [7] D. Zhu, K. Li, C. C. Faraco, F. Deng, D. Zhang, L. Guo, L. S. Miller, and T. Liu, “Optimization of functional brain ROIs via maximization of consistency of structural connectivity profiles,” *NeuroImage*, vol. 59, no. 2, pp. 1382–93, Jan. 2012.
- [8] T. Liu, H. Li, K. Wong, A. Tarokh, L. Guo, and S. T. C. Wong, “Brain tissue segmentation based on DTI data,” *NeuroImage*, vol. 38, no. 1, pp. 114–23, Oct. 2007.
- [9] M. Jenkinson, P. Bannister, M. Brady, and S. Smith, “Improved optimization for the robust and accurate linear registration and motion correction of brain images,” *Neuroimage*, vol. 17, no. 2, pp. 825–841, 2002.